Lepton pair production at the CERN SPS

Adam Winkels
Department of Physics
McGill University
Montréal, Québec
Canada

A thesis submitted to the
Faculty of Graduate Studies and Research
in partial fulfillment of the requirements for the degree of
Master of Science

Dedicated, with thanks, to Fritz and Mary Lou Winkels, for pre- and postnatal moral and financial support, and to Anna Sirdevan, for putting up with numerous mind numbing soliloquies about soups and gases.

Contents

List of Figures

List of Tables

Abstract

We interpret theoretically electron pair data observed in Pb(158 AGeV)-Au collisions at the CERN SPS by considering the system as an evolving fireball with parameters fit to experimental observables. Dilepton production in the QGP phase is found via standard finite temperature field theory techniques where annihilating quarks have thermally generated effective masses. After the phase transition, contributions from ρ and ω meson decays are found via from experimentally determined forward scattering amplitudes which account for the effects of emission from a medium with finite temperature and density. All results are folded with a model which considers bias created by the CERES detector's acceptance. Our calculations agree well with existing data dilepton production at low and intermediate invariant masses.

Résumé

Nous interprétons les données expérimentales sur les paires de leptons mesurées dans les collisions Pb-Au à 158 AGeV, au SPS du CERN. Nous traitons l'évolution du système hadronique en considérant une modélisation thermodynamique ajustée aux observables asymptotiques. La production de leptons dans la phase du plasma quark-gluon est obtenue avec les techniques reconnues de la théorie des champs à température finie, où les quarks ont des masses thermiques non-nulles. Après la transition de phase, les contributions des désintégrations des mésons ρ et ω sont évaluées en partant des amplitudes de diffusion vers l'avant, ce qui tient compte des effets de milieu. Tous nos résultats sont filtrés par l'acceptance du détecteur CERES. Nos calculs sont en accord avec les données mesurées sur la production de dileptons de petite et moyenne masses invariantes.

Acknowledgments

None of the following would have been possibly without the tireless guidance of Charles Gale and Joerg Ruppert. Many thanks also go out to Remi Labrecque, Guangyou Qin, Thorsten Renk and Gojko Vujanovic for very helpful insight, advice and discussion.

1

Introduction

Unsurprisingly, both scientists and laypeople are fascinated by the origins of our species as well as the universe in which we reside. The current common philosophy is that the universe began as an unimaginably small volume of nearly infinite energy and density. This volume began to expand outward and cool, eventually forming the stars and galaxies we observe today. The physical structure of the universe during the very early moments of this expansion was vastly different than its current state: due to the volume's extremely large energy density and temperature the quarks and gluons, which would later form the internal structure of the hadrons which make up everyday matter, were instead deconfined in a phase of matter known as quark-gluon plasma (QGP).

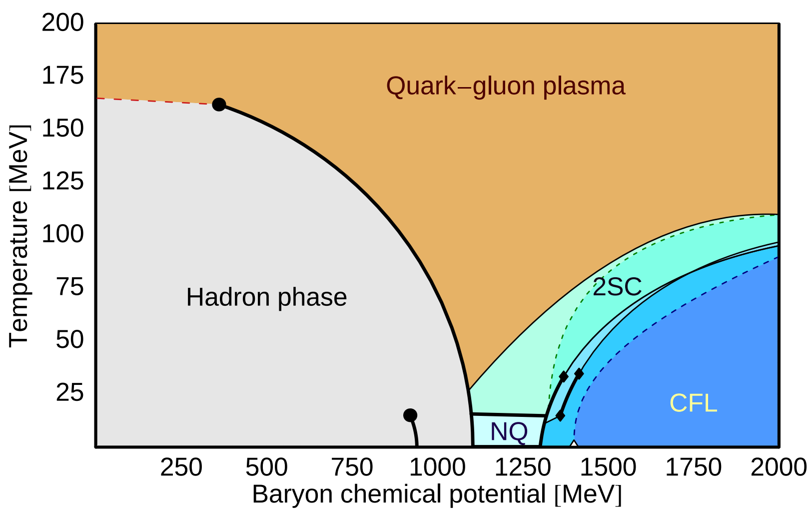

Figure 1.1: The QCD phase diagram (from [1]).

This novel state of matter is of interest not only because of its supposed presence in the very early life of the universe, but as a prediction of quantum chromodynamics (QCD) [6] its existence and properties serve as an important test of the standard model. In fact, the QGP is merely one component of the so-called QCD phase diagram, which attempts to detail the behaviour of strongly interacting matter over a wide range of temperatures and chemical potentials (μ). An example of the diagram is given in Figure 1.1, though this is merely a schematic view; establishing the exact temperatures, pressures, and orders of transition is still an energetic field of study for both theoretical and experimental physicists. This diagram does, however, contain fascinating clues on the many phases that are thought to exist in finite-temperature and density QCD. Among these are domains like colour-flavour-locking (CFL) and 2SC that are colour-superconduncting phases: these may be important for the cooling properties of neutron stars. In this thesis our interest will be restricted to the hadron and quark-gluon plasma domains.

Significant effort has been expended attempting to recreate the QGP in a laboratory setting. Given the energy required to produce the conditions necessary for a phase transition, much of this work has been focused on relativistic heavy ion collisions, where the momentum and masses of the incident particles are sufficient to create the deconfined plasma. It is believed that the QGP has been created in experiments at facilities including the Relativistic Heavy Ion Collider (RHIC), located at the Brookhaven National Laboratory, and possibly at the European Organization for Nuclear Research (CERN) Super Proton Synchrotron (SPS). The QGP is also expected to be created at the soon-to-be online Large Hadron Collider (LHC). However, to date there are no results which convincingly confirm that experiments have indeed created this phase. Furthermore, merely reproducing the QGP does not in and of itself supply the insight necessary for a complete picture of the process of deconfinement, as one also requires the tools necessary to study the internal physics of the plasma. Given that the lifetime of the strongly interacting phase is thought to be on the order of a few fm/c (about 10^{-23} seconds), and has a diameter of about same extent in fm, probes hoping to confirm and characterize the QGP must be carefully

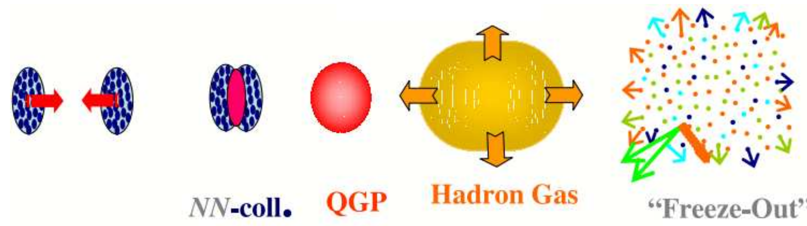

Figure 1.2: A schematic depiction of heavy ion collisions (from [2]). After the incident nuclei collide (2nd frame), the constituent particles scatter off of one another, resulting in the system quickly reaching thermal equilibrium. Should the collision be energetic enough, the partons in the equilibrated system will become deconfined, forming a quark-gluon plasma (3rd frame). Thermal pressure causes the system to expand and cool, resulting in reconfinment of quarks and gluons into a gas of hadrons (4th frame). The volume continues to expand and particles continue to rescatter until their mean free path exceeds the system size (5th frame), after which interactions cease.

selected so as to be suitable in this regime. Various observables have been proposed and studied, including J/Ψ suppression [7] and strangeness enhancement [8], as signals of deconfinement, and disoriented chiral condensates to explore chiral symmetry restoration [9]. While these are well worthy of study, we choose to focus on electromagnetic emissions, in the form of real photons and dileptons (e^+e^- or $\mu^+\mu^-$ pairs) from virtual photons. This class of probes has the distinct advantage of being color neutral, allowing them to escape the collision volume without undergoing significant final state interactions. This near invulnerability to the strong force which dominates the partonic phase makes EM probes ideal as a signal of deconfinement as well as helping to illuminate the kinematical properties of the collision at early times.

To motivate the origins of these electromagnetic probes, it is pertinent to provide an overview of the collision process: after the initial impact, the bulk of the constituent particles cannot immediately escape the volume (often referred to as the *fireball*); instead, they rescatter off of one another, causing the system to quickly thermalize. If the incident ions contain sufficient energy, the thermalized system will be hot enough to transform the bulk into the strongly interacting system we refer to as the quark-gluon plasma. Such a state exists only for a short time, as the thermal pressure within causes the volume to expand and cool. Once reaching the critical temperature $T_C \approx 170$ MeV [10], the partons become reconfined, coalescing into hadrons in an event appropriately named *hadronization*, after which the volume continues its expansion.

Note that hadronization is not understood theoretically, as QCD is a strongly-coupled theory and the energy scale at which this occurs lies in the non-perturbative regime. Its description must therefore rely on empirical observations and measurement. The newly formed particles rescatter until the mean free path of the hadrons is greater than typical interparticle distances, at which point they decouple, a process known as *freeze-out*. After this time, all that remains of the collision are hadron resonances, which have been well studied in other, lower energy heavy ion experiments.

When studying dilepton radiation from heavy ion collisions, one must consider the entire lifetime of the collision presented in Figure 1.2. In the QGP phase, the dominant source of lepton pair creation is via quark-antiquark annihilation, $q\overline{q} \to \gamma \to l^+l^-$, while after the phase transition we are most likely to see dileptons created from meson decays. In order to reproduce the dilepton production data obtained from heavy ion experiments, a method is needed to model the pair creation in these sectors. This requires an understanding not only of processes that create the spectra, but the physics of the volume over its life span. Given the many particles and significant energies that go into these experiments, such a task appears daunting. However, in this work we will employ a set of methods which simplifies the process in order to study dilepton rates for one class of collisions, 158 AGeV Pb-Au, which have been performed at the CERN SPS, and measured by the CERES collaboration. Firstly, we characterize quarks and gluons in the partonic phase as a gas of quasiparticles heavily influenced by thermal interactions while in the hadronic phase, we calculate pair production via a method which determines the forward scattering amplitude of ρ and ω mesons from measured data. To reproduce the experimental dilepton measurements, which consider the entire lifetime of the fireball, we employ a model which emulates and simplifies the results of hydrodynamical simulations in order to produce a compact description of the collision evolution. This description has previously been successful in reproducing the dilepton spectra from In-In collisions found from the NA60 experiment at the CERN SPS [11]: it is our goal to obtain a consistent theoretical description of dilepton emission at the CERN SPS.

This work is presented as follows: in Chapter 2 we outline the method used to describe the thermodynamic and kinematic evolution of the collision. Chapter 3 outlines the techniques needed to calculate dilepton production from the different phases of the evolving medium. In Chapter 4 we describe our model of the detector acceptance and our method of numerically evaluating pair production before presenting the results obtained. The final chapter looks back at our approach and discusses future subjects of study and modifications which could be of interest.

2

System Evolution

Our approach to reproducing dilepton radiation from heavy ion collision can be expressed schematically by [12]

$$\frac{dN}{dM\,dp_T\,d\eta} = \text{evolution} \otimes \frac{dN}{d^4x d^4q} \otimes \text{acceptance} \tag{2.1}$$

that is, a convolution of the dynamics of the evolving thermalized system created by the collision with the differential pair creation rate for the different phases, folded with a model of the detector acceptance. If the created volume is indeed a deconfined plasma which transitions to a hot hadronic gas, this construction should accurately reproduce experimental data. The first component, the evolution, is discussed below, including theories necessary for its function.

2.1 Quasiparticle Model

In attempting to model the behaviour of heavy-ion collisions, one of the most difficult challenges is describing the thermodynamics of the quark-gluon plasma. Any approach hoping to determine the equation of state (EoS) in this domain must address the new degrees of freedom caused by the deconfined nature of quarks and gluons at high energy density and pressure. Studies utilizing perturbative QCD techniques have yielded useful results; however, these break down due to the large coupling at the energy scales presently probed by experiments [13]. A more complete picture, with results spanning the phase transition, has been developed using lattice QCD. Stemming from this work have been attempts to develop a phenomenological description of the thermodynamics near T_C, usually adapting the quasiparticle approach first utilized in solid state physics. When applied in the regime of the QGP, this technique gives us quasifree quarks and gluons with dynamics and properties heavily influenced by interactions with surrounding particles. We take advantage of one such description, put forth by Schneider and Weise [14], to describe the EoS of the quark-gluon plasma.

This approach proposes that if the momenta of these constituent quasiparticles satisfies $k \sim T$, then Hard Thermal Loop (HTL) methods [15] can be used to determine the thermal quasiparticle masses, given by

$$\frac{m_g(T)}{T} = \sqrt{\frac{N_c}{6} + \frac{N_f}{12}}\tilde{g}(T, N_C, N_f)^2 \tag{2.2}$$

and

$$\frac{m_q(T)}{T} = \sqrt{\left(\frac{m_q^0}{T} + \frac{1}{4}\sqrt{\frac{{N_C}^2 - 1}{N_C}}\tilde{g}(T)\right)^2 + \frac{{N_C}^2 - 1}{16 N_C}\tilde{g}(T)^2} \tag{2.3}$$

for gluon and quark particles, respectively. The effective coupling $\tilde{g}$ is

$$\tilde{g}(T, N_C, N_f) = \frac{g_0}{\sqrt{11 N_C - 2 N_f}}\left(1 + \delta - \frac{T_C}{T}\right)^{\gamma} \tag{2.4}$$

where N_C is the number of colours, N_f the number of flavours and m_q^0 the bare quark mass. Furthermore, g_0, δ and γ are parameters which can be gleaned from lattice simulations. For this work, we set $g_0 = 9.4$, $\delta = 10^{-6}$ and $\gamma = 0.1$, which the original authors derived by matching their model with recent results [16].

In this quasiparticle description, the relevant thermodynamic properties of the quark-gluon plasma are given by

$$p(T) = \frac{v_g}{6\pi^2}\int_0^\infty dk[C(T) f_B(E_k^g)]\frac{k^4}{E_k^g} + \sum_{i=1}^{N_f}\frac{2N_C}{3\pi^2}\int_0^\infty dk[C(T) f_D(E_k^i)]\frac{k^4}{E_k^i} - B(T) \tag{2.5}$$

$$\epsilon(T) = \frac{v_g}{2\pi^2}\int_0^\infty dkk^2[C(T)f_B(E_k^g)]E_k^g + \sum_{i=1}^{N_f}\frac{2N_C}{\pi^2}\int_0^\infty dkk^2[C(T)f_D(E_k^i)]E_k^i + B(T) \tag{2.6}$$

$$\begin{aligned} s(T) = {} & \frac{v_g}{2\pi^2 T}\int_0^\infty dkk^2[C(T)f_B(E_k^g)]\frac{\frac{4}{3}k^2 + m_g^2(T)}{E_k^g} \\ & + \sum_{i=1}^{N_f}\frac{2N_C}{\pi^2 T}\int_0^\infty dkk^2[C(T)f_D(E_k^i)]\frac{\frac{4}{3}k^2 + m_i^2(T)}{E_k^i} \end{aligned} \tag{2.7}$$

where $m_g(T)$ and $m_i(T)$ are the thermal gluon and quark masses and $p(T), \epsilon(T)$ and $s(T)$ correspond to the pressure, energy density and entropy density, respectively. The functions $f_B(E)$ and $f_D(E)$ refer to the Bose-Einstein and Fermi-Dirac distributions with zero baryon chemical potential, while we signify the gluon energy by $E_k^g = \sqrt{k^2 + m_g^2(T)}$ and the quark energy, for flavour $q = i$, by $E_k^i = \sqrt{k^2 + m_i^2(T)}$. Furthermore, we have the temperature dependent functions B(T) and C(T), given by

$$B(T) = B_1(T) + B_2(T) + B_0 \tag{2.8}$$

where

$$\begin{aligned} B_1(T) = {} & \frac{v_g}{6\pi^2}\int_{T_C}^T d\tau \frac{dC(\tau)}{d\tau}\int_0^\infty dk f_B(E_k^g)\frac{k^2}{E_k^g} \\ & + \sum_{i=1}^{N_f}\frac{2N_C}{3\pi^2}\int_{T_C}^T d\tau \frac{dC(\tau)}{d\tau}\int_0^\infty dk f_D(E_k^i)\frac{k^2}{E_k^i} \end{aligned} \tag{2.9}$$

and

$$\begin{aligned} B_2(T) = {} & -\frac{v_g}{4\pi^2}\int_{T_C}^T d\tau C(\tau)\frac{dm_g^2(\tau)}{d\tau}\int_0^\infty dk f_B(E_k^g)\frac{k^2}{E_k^g} \\ & + \sum_{i=1}^{N_f}\frac{N_C}{\pi^2}\int_{T_C}^T d\tau C(\tau)\frac{dm_i^2(\tau)}{d\tau}\int_0^\infty dk f_D(E_k^i)\frac{k^2}{E_k^i} \end{aligned} \tag{2.10}$$

with B_0 determined by the necessity that the system pressure at T_C is equal for both phases. Finally, we have

$$C(T) = C_0 \left([1 + \delta_c] - \frac{T_C}{T} \right)^{\beta_C} \tag{2.11}$$

where the included parameters are set to $C_0 = 1.16, \delta_C = 0.02$ and $\beta_C = 0.29$.

It is worth noting that Schneider and Weise's interpretation includes another relevant proposal, that is, that the function $C(T)$ can be interpreted as a phenomenological method of accounting for the change in the number of thermally active degrees of freedom caused by transitioning to or from the quark-gluon plasma phase. They suggest that, in addition to being included in the QGP equation of state, $C(T)^2$ (referred to in this application as the *confinement factor*) should be applied to the differential pair production rate as a method of modelling the macroscopic effects of confinement on dilepton emission. When implemented in this manner, the confinement factor causes, on average, an order of magnitude decrease in the dilepton rates. Results presented later in this work indicate that a reduction of this scale would lead to significant deviation from the data collected at CERES and, in fact, Schneider and Weise have expressed theoretical after-thoughts which cast doubt in this interpretation. Given these facts, we omit $C(T)$ from the production rates and choose to interpret its presence in the aforementioned quasiparticle thermodynamics as merely necessary to fit results with those put forth by lattice simulations.

2.2 Fireball Evolution Model

2.2.1 Quark-Gluon Phase

Modelling the dynamics and observables resulting from collision is a crucial component in the study of heavy-ion collisions. Data collected from the CERES experiment includes particle rates over the entire lifetime of the fireball, from thermalization to freeze-out, and it is not currently possible for the detector to discern from which temperature or phase domain particular counts were emanated. Furthermore, the dynamics of the medium from which dileptons are emitted has a drastic effect on their observable properties. Thus, for it to be possible to compare a model of heavy ion collisions to experimental results, one requires a description of the evolution of the post-collision volume. Attempts at depicting the evolution are frequently based on adapting knowledge gained through the oft-studied discipline of hydrodynamics. This methodology, as it applies to heavy ion collisions, is based on the assumption that the system created is in a sufficient enough thermal equilibrium, at least locally, that the interactions between constituent particles cause the volume to expand and flow as a fluid. At its base level, this description is encapsulated by the equation [17]

$$\partial_\mu T^{\mu\nu} = 0 \tag{2.12}$$

where $T^{\mu\nu}$ is the stress energy tensor, which in hydrodynamics is given by

$$T^{\mu\nu} = (\epsilon + P)u^\mu u^\nu - P g^{\mu\nu} \tag{2.13}$$

with energy density ϵ, flow four-velocity $u^\mu = (t, \mathbf{x})$ ($u^\mu = (1,0,0,0)$ in the fluid's rest frame), pressure P and $g^{\mu\nu}$ representing the Minkowski metric. The simplicity of the above equations is misleading, however, as in practice the mathematics of hydrodynamical expansion grow significantly in complexity with deeper analysis, causing integration of this approach into numerical simulations to be extremely resource intensive, especially if one wishes to use a Monte Carlo to simulate detector acceptance, as we will later do. To avoid these potential complications, we employ the model of an expanding fireball proposed by Renk [3][4][18], which incorporates the work of Schneider and Weise, to describe the evolution of the system. Rather than attempting to detail the system's motion and characteristics for each hydrodynamic cell, Renk sets forth an idealized approach which aims to parameterize the expansion and extract from it observables relevant to the study of the QGP in heavy ion collisions.

This model contains a few significant assumptions: firstly, the expansion is simplified by assuming that the fireball physics are uniform over the entire system for each slice of proper time τ. In the center of mass frame, the fireball is cylindrical with accelerated expansion occurring isentropically away from the point of collision, though relativistic effects are only considered along the longitudinal axis. After some initial time τ_0 the entire volume is assumed to be in local thermal equilibrium until τ_f, the time of freeze out, when the mean free path of the constituent particles exceeds the size of the fireball, after which no significant interactions occur.

We will briefly outline how the model calculates expansion parameters, beginning with the transverse flow [4]: at a given proper time the transverse rapidity $\rho = \mathrm{atanh}(v_T(\tau))$ is assumed to be linearly related to the radial coordinate r by

$$\rho = \frac{r\rho_c(\tau)}{R_c(\tau)} \tag{2.14}$$

where r is scaled by the transverse rapidity $\rho_c(\tau) = \mathrm{atanh}(a_T\tau)$ and radius $R_c = R_0 + \frac{a_T}{2}\tau^2$ (where R_0 is the initial overlap radius) along a certain acceleration path given by the parameter a_T. This acceleration path is found through analysis of longitudinal expansion, whose evolution cannot be so succinctly defined: though the freeze out velocity of the expansion front, v_f^{front}, can be uniquely determined by experimental measurements of the front momentum rapidity, η_f^{front} (where $\eta = \frac{1}{2}\ln\frac{p_0+p_z}{p_0-p_z}$), there are no such observables corresponding to the velocity at thermalization, v_0^{front}. However, by demanding that the velocity at τ_f has evolved to match the measured rapidity, i.e. $\mathrm{atanh}(v_{f,\mathrm{evo}}^{front}) = \eta_{f,\mathrm{exp}}^{front}$, the longitudinal flow can be calculated by integrating the velocity and length over all possible acceleration paths and then determining which possibility will lead to homogeneous expansion [12]. Under this prescription, the longitudinal extension for a given proper time can be given as

$$L(\tau) \approx 2\tau \frac{\sinh(\zeta(\tau)-1)\eta_S^{front}}{(\zeta(\tau)-1)} \tag{2.15}$$

where $\zeta(\tau) = \frac{\eta^{front}(\tau)}{\eta_s^{front}(\tau)}$, which takes accounts for difference in spacetime rapidity η_s and momentum rapidity η caused by the accelerating expansion.

The radial expansion is assumed to follow

$$R(\tau) = R_0 + c_T \int_{\tau_0}^{\tau} d\tau' \int_{\tau_0}^{\tau'} d\tau'' \frac{p(\tau'')}{\epsilon(\tau'')} \tag{2.16}$$

where R_0 is a constant found via initial nuclear overlap calculations using the Glauber model and c_T is a parameter related to a_T. $p(\tau)$ and $\epsilon(\tau)$ are the pressure and entropy density, respectively, and are determined by the quasiparticle EoS. The combination of (2.15) and (2.16) in concert with the assumed cylindrical shape gives us the time-dependent volume $V(\tau) = \pi R(\tau)^2 L(\tau)$.

Given that we have assumed isentropic expansion, the condition $s = \frac{S_0}{V(\tau)}$ is combined with the quasiparticle equation of state to iteratively solve the thermodynamic properties of the fireball in the QGP phase.

2.2.2 Hadronic Phase

For temperatures above T_C, the thermodynamics of the fireball are well described by using the quasiparticle model outlined previously. The temperature region from around the phase transition to freeze out at T_f, however, is problematic, as a quasi-particle description is no longer applicable and lattice simulations in this domain produce unphysically large particle masses. This is addressed by assuming the creation of a non-interacting, chemically equilibrated system of hadrons describing the hadron resonance gas created at freeze-out [3]. Although such a description would not be accurate for the hadronic phase that exists from τ_C to τ_f, knowledge of the system at these two points can be used to fit thermodynamic properties for the interlying region. Using the observed inequality of quarks and antiquarks at the CERN SPS, one can infer the presence of a temperature dependent baryon chemical potential, μ_B, which can be experimentally determined at τ_f by analyzing observed particle ratios [19]. As mentioned previously, the fireball model assumes isentropic expansion over its entire lifetime with the total entropy being a known quantity. This, in addition to imposed baryon number conservation and knowledge of the thermodynamic evolution of an ideal hadron gas, gives the ability to set a fixed point at T_f, from which the thermodynamics of the system can be interpolated back to the phase transition (see Figure 2.1). With knowledge of the equation of state in the hadronic phase, the system evolution can be computed as described in the previous section.

Using the concepts of statistical hadronization [20], the evolution calculated by this approach has been shown [18] to reproduce measured hadron resonance ratios to a high degree of accuracy if one includes a finite pion chemical potential created at the crossover that rises approximately linearly to a value of $\mu_\pi = 110\text{MeV}$ at freeze

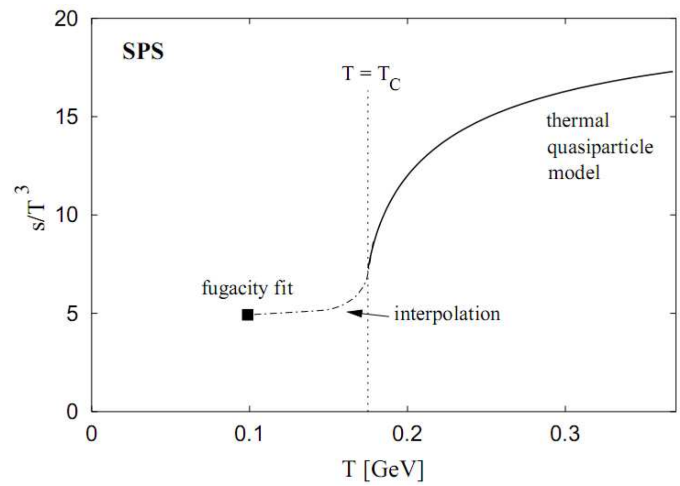

Figure 2.1: Entropy density from the fireball evolution model at for collisions at the SPS. Interpolation is shown in the hadronic phase, from the quasiparticle value to freeze out (point labelled "fugacity fit"), computed by imposing baryon number and entropy conservation (from [3]).

out.

2.2.3 Model Parameters

Most of the parameters necessary to compute the fireball evolution can be obtained via calculation or experimental data. For example, the baryon and strange chemical potentials in the hadronic phase can be uniquely determined by the number of participant baryons and the fireball volume, which in turn is found via the total system entropy, determined by experiment, and the entropy density at T_C, determined by lattice simulations. The parameters that cannot be determined thusly are the initial volume front rapidity $\eta_f(\tau_0)$, the final transverse velocity $v_T(\tau_f)$ and the freeze-out temperature. Instead, the values are tweaked so as to best match the evolution with existing results for the hadronic momentum spectra and Hanbury-Brown Twiss (HBT) correlations (see Figure 2.2). We stress here an important point: even though we are seeking to theoretically interpret electromagnetic data, our fireball parameters are perfectly consistent with, and in fact determined by, *hadronic* measurements.

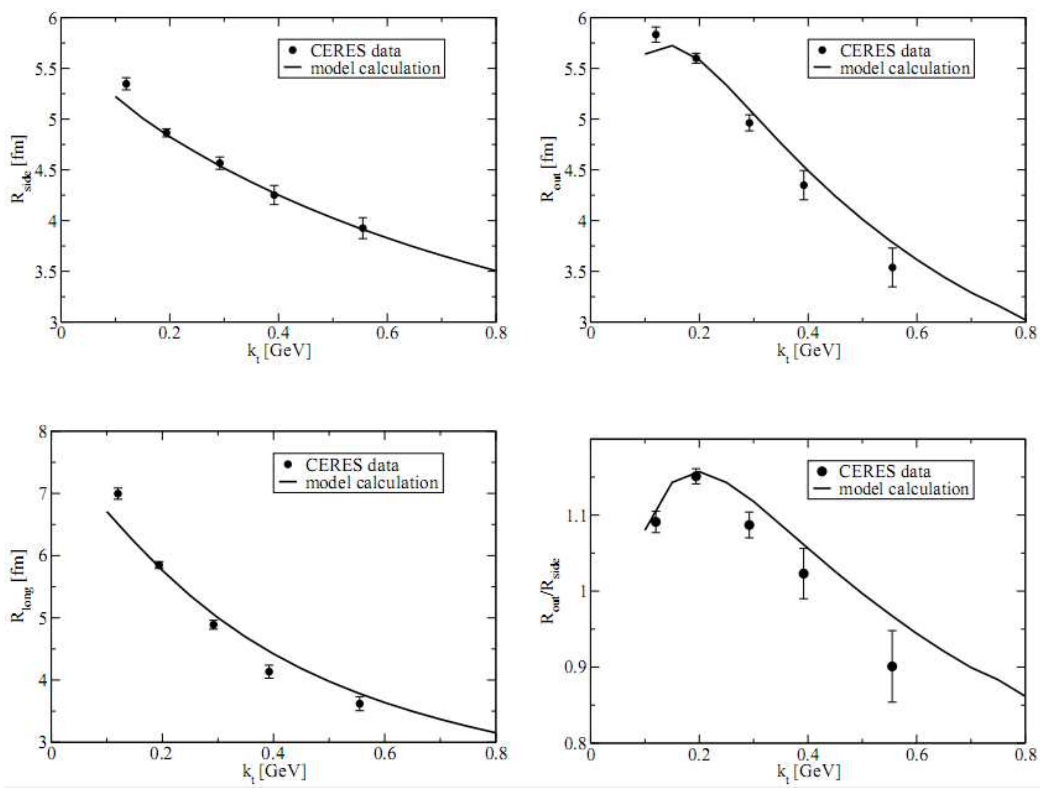

Figure 2.2: Comparison of evolution HBT radii as a function of transverse pair momentum to CERES experimental data (from [4]).

3

Dilepton Production

The differential lepton pair production rate from a virtual particle with four-momentum q in a thermalized medium can be written as [3]

$$\frac{dN}{d^4x d^4q} = \frac{\alpha^2}{\pi^3 q^2} \frac{1}{e^{\frac{q^0}{T}} - 1} \mathrm{Im}\overline{\Pi} \tag{3.1}$$

where lepton masses have been neglected, α is the fine structure constant and $\overline{\Pi} = -\frac{\Pi^\mu_\mu}{3}$ is the trace over the retarded photon self-energy at finite-temperature. The above equation is known to be valid to order α for electromagnetic interactions and all orders for strong interactions.

The thermal self-energy of the l^+l^- decay parent is clearly of great importance, but the nature of this particle varies depending on the stage of evolution one is analyzing. Here we will discuss the spectral functions relevant for each phase domain.

3.1 Dileptons from the QGP Phase

3.1.1 Finite Temperature Field Theory Approach

Given that lepton-antilepton pairs in the QGP originate via virtual photons created by quark-antiquark annihilation, analysis of the pair production rate in this phase requires the thermal photon self energy. At the one-loop level, this quantity can be obtained using standard thermal field theory techniques [15]. We begin with the Schwinger-Dyson equation

$$\Pi_{\mu\nu} = D^{-1}_{\mu\nu} - D_{0\,\mu\nu}^{-1} \tag{3.2}$$

where $D_{\mu\nu}^{-1}$ and $D_{0\mu\nu}^{-1}$ are the full and bare inverse photon propagators, respectively. Substituting these values gives

$$\Pi^{\mu\nu} = e^2 T \sum_l \int \frac{d^3p}{(2\pi)^3} \mathrm{Tr}\left(\gamma^\nu \frac{1}{\not{p} - m} \gamma^\mu \frac{1}{\not{p} + \not{k} - m}\right) \tag{3.3}$$

where k is the photon four-momentum, p is the virtual particle momentum and we use the thermal-field theory definitions $p^0 = (2l+1)\pi T i + \mu$ and $k^0 = 2n\pi T i$, involving the well-known discrete Matsubara frequencies. The above is obtained in Quantum Electrodynamics (QED), at one loop. Separating the vacuum contribution from the relevant in-medium result gives

$$\Pi^\mu_\mu(k_0, \omega) = -2\frac{e^2}{\pi^2}\mathrm{Re}\int_0^\infty dp \frac{p^2}{E_p} N_F(p)\left[1 - \frac{2m^2 + k^2}{4p\omega}\ln\left(\frac{R_+}{R_-}\right)\right] \tag{3.4}$$

where

$$\omega = |\mathbf{k}|,\ k^2 = k_0^2 - \omega^2,\ E_p = \sqrt{\mathbf{p}^2 + m^2},\ \beta = \tfrac{1}{T}$$
$$N_F(p) = \tfrac{1}{e^{\beta(E_p - \mu)}+1} + \tfrac{1}{e^{\beta(E_p+\mu)}+1},\ R_\pm = k^2 - 2k_0 E_p \pm 2p\omega$$

and the Re operator takes the definition $\mathrm{Re}(f(k^0)) = \frac{1}{2}[f(k^0) + f(-k^0)]$, as the presence of the thermal medium means that Lorentz invariance is no longer manifest. Evaluating the integral, converting to the form presented in (3.1) and finding the imaginary contribution at vanishing baryon chemical potential gives

$$\begin{aligned} \mathrm{Im}\overline{\Pi}(k_0, \omega) = {} & \frac{k^2}{12\pi} 3 \sum_{f=u,d,s} \theta(k^2 - 4{m_f}^2){e_f}^2\left(1 + \frac{2{m_f}^2}{k^2}\right)\sqrt{1 - \frac{4{m_f}^2}{k^2}} \\ & \times \left\{ \frac{2T}{\omega} \frac{1}{\sqrt{1 - \frac{4{m_f}^2}{k^2}}} \ln\left(\frac{f_D\left(\frac{k_0}{2} - \frac{\omega}{2}\sqrt{1 - \frac{4{m_f}^2}{k^2}}\right)}{f_D\left(\frac{k_0}{2} + \frac{\omega}{2}\sqrt{1 - \frac{4{m_f}^2}{k^2}}\right)} \right) - 1 \right\} \end{aligned} \tag{3.5}$$

where $f_D(E) = \frac{1}{e^{\frac{E}{T}}+1}$ is the Fermi-Dirac distribution function and m_f is the quark (antiquark) thermal mass. Eq. (3.5) can be inserted in to (3.1) to generate dilepton production rates, as shown in Figure 3.1. As expected, this figure shows greater dilepton production at higher temperatures where we are more likely to see quark-antiquark

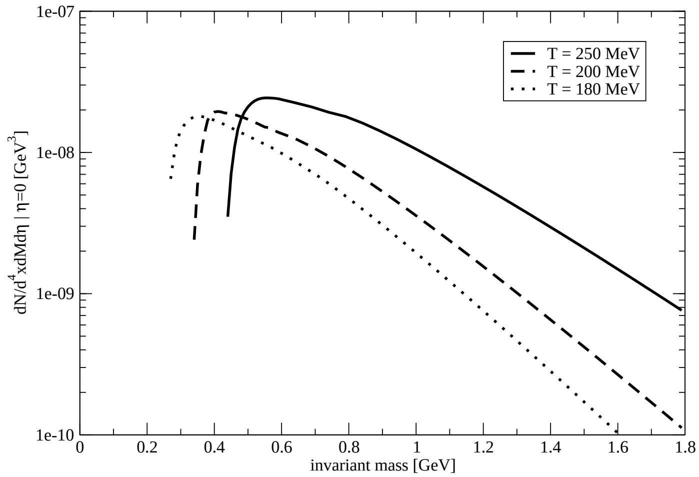

Figure 3.1: Dilepton production rates from the QGP phase generated using our field theory approach with effective masses (see (2.3)) at different temperatures.

annihilations. Also note the significant effect caused by the inclusion of thermally generated masses, which manifest in the form of sharp, temperature-dependent rate cutoffs. This phenomena will be discussed in more detail in Section 4.3 when we discuss its impact on observable data.

3.1.2 Kinetic Theory Approach

As a check of this approach and the numerical routines we later utilize, we also consider a method of calculating dilepton emission via kinetic theory, as put forth by Kajantie et al. [21]. For quark-antiquark annihilation, we have the cross section

$$\sigma(M) = F_q \tilde{\sigma}(M) \tag{3.6}$$

This is based off the well known result for $e^+e^- \rightarrow \mu^+\mu^-$, where

$$F_q = N_C(2s+1)^2 \sum_f e_f^2 \tag{3.7}$$

which accounts for the fractional charge and spin of the quarks. The electron-muon cross section can be calculated via elementary quantum electrodynamics (for example, see [22]), from which we find, for identical incident particles in the center of mass frame,

$$\frac{d\sigma}{d\Omega} = \frac{1}{4M^3}\frac{|\mathbf{k}|}{2\pi^2}\frac{1}{4}\sum_{spins}|\mathcal{M}(p_1, p_2 \to k_1, k_2)|^2 \tag{3.8}$$

where $\mathbf{k}$ is the three-momentum of a created muon and $\frac{1}{4}\Sigma_{spins}|\mathcal{M}|^2$ is the spin-averaged matrix element for the process. Inserting these quantities and integrating over the solid angle gives the total cross section, with lepton mass m_l:

$$\tilde{\sigma}(M) = \frac{4\pi}{3}\frac{\alpha^2}{M^2}\left(1 + \frac{2m_l^2}{M^2}\right)\sqrt{1 - \frac{4m_l^2}{M^2}} \tag{3.9}$$

From kinetic theory, we have the dilepton creation rate

$$\frac{dN}{d^4x} = \int \frac{d^3p_1}{(2\pi)^3} f(\mathbf{p}_1) \int \frac{d^3p_2}{(2\pi)^3} f(\mathbf{p}_2)\sigma(q^+q^- \to l^+l^-; \mathbf{p}_1, \mathbf{p}_2)v_{rel} \tag{3.10}$$

where $v_{rel} = \frac{[(p_1 \cdot p_2)^2 - m_a{}^4]^{\frac{1}{2}}}{E_1 E_2}$ and $f(\mathbf{p})$ is the occupation probability. Kajantie et al. propose that, in this context, the quantum effects in the pair creation are negligible and we should instead focus on the relativistic effects. This leads to the simplification

$$f(\mathbf{p}) \approx \mathrm{e}^{-\frac{\sqrt{\mathbf{p}^2 + m_q^2}}{T}} = \mathrm{e}^{-\frac{E}{T}}$$

that is, a Maxwell-Boltzmann distribution, where we consider only the energy of the particles while disregarding the issues of state occupation present in Fermi-Dirac statistics.

To determine the differential rate in M and p_T we drop the quark mass, which should be acceptable for a comparison using only the two lightest quark flavours, and introduce a δ function, giving

$$\begin{aligned}
\frac{dN}{d^4x dM^2} &= \int \frac{d^3p_1}{(2\pi)^2}\sigma(M)\frac{d^3p_2}{(2\pi)^2}\frac{(p_1 \cdot p_2)}{E_1 E_2}\mathrm{e}^{-\frac{E_1}{T}}\mathrm{e}^{-\frac{E_2}{T}}\delta(M^2 - (p_1 + p_2)^2) \\
&= \frac{M^2\sigma(M)}{2}\int \frac{d^3p_1}{(2\pi)^2}\frac{d^3p_2}{(2\pi)^2}\frac{1}{E_1 E_2}\mathrm{e}^{-\frac{E_1}{T}}\mathrm{e}^{-\frac{E_2}{T}}\delta(M^2 - 2p_1 \cdot p_2) \\
&= \frac{M^2\sigma(M)}{(2\pi)^4}\int d|\mathbf{p_1}|d|\mathbf{p_2}|d\zeta\mathbf{p_1}^2\mathbf{p_2}^2\frac{1}{E_1 E_2}\mathrm{e}^{-\frac{E_1}{T}}\mathrm{e}^{-\frac{E_2}{T}}\delta(M^2 - 2E_1E_2 + 2|\mathbf{p_1}||\mathbf{p_2}|\zeta)
\end{aligned} \tag{3.11}$$

where ζ is the cosine of the angle between the incident quarks. We adjust the Dirac delta to give

$$\delta(M^2 - 2E_1E_2 + 2|\mathbf{p_1}||\mathbf{p_2}|\zeta) = \frac{\delta(\zeta - \zeta_0)}{2|\mathbf{p_1}||\mathbf{p_2}|} \tag{3.12}$$

$$\zeta_0 = \frac{2E_1E_2 - M^2}{2|\mathbf{p_1}||\mathbf{p_2}|}$$

Inserting this into Eq. (3.11) removes an integral and gives

$$\frac{dN}{d^4x dM^2} = \frac{M^2\sigma(M)}{2(2\pi)^4} \int |\mathbf{p_1}|d|\mathbf{p_1}||\mathbf{p_2}|d|\mathbf{p_2}| \frac{1}{E_1E_2} \mathrm{e}^{-\frac{E_1}{T}} \mathrm{e}^{-\frac{E_2}{T}} \tag{3.13}$$

and given $|\mathbf{p}|d|\mathbf{p}| = EdE$, this becomes

$$\frac{dN}{d^4x dM^2} = \frac{M^2\sigma(M)}{2(2\pi)^4} \int dE_1 dE_2 \mathrm{e}^{-\frac{E_1}{T}} \mathrm{e}^{-\frac{E_2}{T}} \tag{3.14}$$

This fairly straightforward integration gives the differential mass spectra

$$\frac{dN}{d^4x dM} = \frac{\sigma(M)}{(2\pi)^4} M^4 T K_1\left(\frac{M}{T}\right) \tag{3.15}$$

where K_1 is a modified Bessel function of the second kind. A very similar approach can be used to determine the dilepton transverse momentum spectra:

$$\frac{dN}{d^4x dM dp_T} = \frac{\sigma(M)}{2(2\pi)^4} M^3 p_T K_0\left(\frac{E_T}{T}\right) \tag{3.16}$$

where $E_T = \sqrt{p_T^2 + M^2}$ is the transverse energy. If one cannot neglect the quark masses (for example, if we consider effective masses caused by thermal interactions), they can be re-inserted by attaching a factor of $1 - 4m_q^2/M^2$.

3.1.3 Further Analysis of Particle Distribution Functions

Despite the vastly different approaches taken in deriving equations (3.5) and (3.15), one can show that the end results only diverge due to the use of different particle occupation probabilities. The kinetic theory approach initially used a Maxwell-Boltzmann distribution; we will now replace this with the analogue from Fermi-Dirac statistics, which is more appropriate when considering systems with quantum effects. Starting from (3.14), which assumes negligible quark masses, we instead have

$$\frac{dN}{d^4x dM^2} = \frac{M^2\sigma(M)}{2(2\pi)^4}\int dE_1 dE_2 \frac{1}{\mathrm{e}^{\frac{E_1}{T}}+1}\frac{1}{\mathrm{e}^{\frac{E_2}{T}}+1} \tag{3.17}$$

The change of variables $x = E_1 + E_2$ and $y = E_1 - E_2$ leads to

$$\begin{aligned}\frac{dN}{d^4x dM^2} &= \frac{M^2\sigma(M)}{4(2\pi)^4}\int_M^\infty dx \int_{-\sqrt{x^2-M^2}}^{\sqrt{x^2-M^2}} dy \frac{1}{\mathrm{e}^{\frac{x+y}{2T}}+1}\frac{1}{\mathrm{e}^{\frac{x-y}{2T}}+1} \\ &= \frac{M^2 T\sigma(M)}{2(2\pi)^4}\int_M^\infty \frac{1}{\mathrm{e}^{\frac{x}{T}}-1}\left[\ln\left(\frac{\mathrm{e}^{\frac{x}{2T}}+\mathrm{e}^{\frac{-\sqrt{x^2-M^2}}{2T}}}{\mathrm{e}^{\frac{x-\sqrt{x^2-M^2}}{2T}}+1}\right) - \ln\left(\frac{\mathrm{e}^{\frac{x}{2T}}+\mathrm{e}^{\frac{\sqrt{x^2-M^2}}{2T}}}{\mathrm{e}^{\frac{x+\sqrt{x^2-M^2}}{2T}}+1}\right)\right]\end{aligned} \tag{3.18}$$

which is not readily soluble analytically. This can be compared to the field temperature dilepton rate by starting from (3.1)

$$\frac{dN}{d^4x d^4q} = \int d^4q \frac{\alpha^2}{\pi^3 q^2}\frac{1}{\mathrm{e}^{\frac{q^0}{T}}-1}\mathrm{Im}\overline{\Pi} \tag{3.19}$$

which can be put in the form of (3.18) using

$$\begin{aligned}\frac{dN}{d^4x dM^2} &= \int\left(\frac{\alpha^2}{\pi^3 q^2}\frac{1}{\mathrm{e}^{\frac{q^0}{T}}-1}\mathrm{Im}\overline{\Pi}\right) d^4q\,\delta(M^2-q^2) \\ &= \int\left(\frac{\alpha^2}{\pi^3 q^2}\frac{1}{\mathrm{e}^{\frac{q^0}{T}}-1}\mathrm{Im}\overline{\Pi}\right) dq_0(4\pi\omega^2)d\omega\,\delta(M^2-q_0^2+\omega^2)\end{aligned} \tag{3.20}$$

where $\omega = |\mathbf{q}|$. Setting $\omega_0 = \sqrt{q_0^2 - M^2}$ gives $\delta(M^2 - q_0^2 + \omega^2) = \frac{\delta(\omega-\omega_0)}{2\omega_0}$ and

$$\begin{aligned}\frac{dN}{d^4x dM^2} &= \int\left(\frac{\alpha^2}{\pi^3 q^2}\frac{1}{\mathrm{e}^{\frac{q^0}{T}}-1}\mathrm{Im}\overline{\Pi}\right) dq_0(4\pi\omega_0^2)\frac{1}{2\omega_0} \\ &= \int(\ldots)dq_0\left(2\pi\sqrt{q_0^2-M^2}\right)\end{aligned} \tag{3.21}$$

Using (3.5) for $\mathrm{Im}\overline{\Pi}$ (assuming a system of only up and down quarks with negligible masses) we find that (3.21), like (3.18), is not analytically soluble; however, both

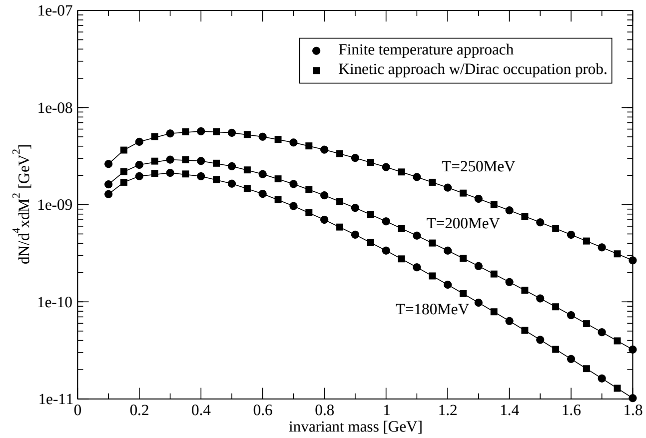

Figure 3.2: Dilepton rates from the QGP phase using kinetic theory with Fermi-Dirac particle occupation and finite temperature field theory approaches, both with neglected quark and lepton masses, for different temperatures.

equations can be easily evaluated numerically. Figure 3.2 presents these results, which indicate that the two techniques are equivalent.

The same conclusion can be reached analytically. Taking, for simplicity, a one flavour system with unit charge, massless quarks and back-to-back lepton pair production, we can expand the logarithm in (3.5) to give

$$\mathrm{Im}\overline{\Pi} = \frac{3M^2}{12\pi}\left(1+\frac{2m_l^2}{M^2}\right)\sqrt{1-\frac{4m_l^2}{M^2}}\left(\frac{\mathrm{e}^{\frac{q_0}{2T}}-1}{\mathrm{e}^{\frac{q_0}{2T}}+1}\right) \tag{3.22}$$

Inserting this into (3.1) becomes

$$\frac{dN}{d^4xd^4q} = \frac{4}{(2\pi)^4}\alpha^2\left(1+\frac{2m_l^2}{M^2}\right)\sqrt{1-\frac{4m_l^2}{M^2}}\left(\frac{1}{\mathrm{e}^{\frac{q_0}{2T}}+1}\right)^2 \tag{3.23}$$

and using $\frac{dN}{d^4xd^4q} = 2M\frac{dN}{d^4xdM^2d^3\mathbf{p}}$ we have

$$\frac{dN}{d^4xdMd^3\mathbf{p}} = \frac{2}{(2\pi)^4}\frac{\alpha^2}{M}\left(1+\frac{2m_l^2}{M^2}\right)\sqrt{1-\frac{4m_l^2}{M^2}}\left(\frac{1}{\mathrm{e}^{\frac{q_0}{2T}}+1}\right)^2 \tag{3.24}$$

Now using kinetic theory, we introduce Dirac deltas to give

$$\frac{dN}{d^4xdM^2d^3\mathbf{p}} = \sigma(M)\int\frac{d^3p_1}{(2\pi)^3}\frac{d^3p_2}{(2\pi)^3}f(\mathbf{p_1})f(\mathbf{p_2})v_{rel}\delta(M^2-(p_1+p_2)^2)\delta(\mathbf{p_1}+\mathbf{p_2}) \tag{3.25}$$

Given the back to back particle creation, we have $\mathbf{p_2} = -\mathbf{p_1}$ and subsequently $E_2 = E_1$, which implies $v_{rel} = \frac{E_1^2+p_1^2}{E_1^2}$. This also allows us to integrate out $\mathbf{p_2}$ dependence, giving

$$\frac{dN}{d^4x dM^2 d^3\mathbf{p}} = \frac{\sigma(M)}{(2\pi)^6} \int d^3p_1 f^2(\mathbf{p}_1) \frac{E_1^2 + \mathbf{p_1}^2}{E_1^2} \delta(M^2 - 4E_1^2) \tag{3.26}$$

Integrating out the angular dependence, transforming the remaining δ-function and realizing for massless quarks $E_1 = |\mathbf{p_1}|$ leaves

$$\frac{dN}{d^4x dM^2 d^3\mathbf{p}} = \frac{\sigma(M)}{2(2\pi)^5} \int E_1 dE_1 f^2(E_1) \delta(E_1 - \frac{M}{2}) \tag{3.27}$$

Given our current assumptions, the cross section is modified by (from (3.7))

$$F_q = N_C (2s+1)^2 \sum_f e_f^2 = (3)(2)^2(\pm 1)^2 = 12 \tag{3.28}$$

Inserting $\sigma(M)$ and evaluating the final integral gives

$$\frac{dN}{d^4x dM^2 d^3\mathbf{p}} = \frac{2}{(2\pi)^4} \frac{\alpha^2}{M} \left(1 + \frac{2m_l^2}{M^2}\right) \sqrt{1 - \frac{4m_l^2}{M^2}} f^2 \left(\frac{M}{2}\right) \tag{3.29}$$

which, for particles obeying a Dirac-Maxwell occupation probability, becomes (given $M = q_0$)

$$\frac{dN}{d^4x dM^2 d^3\mathbf{p}} = \frac{2}{(2\pi)^4} \frac{\alpha^2}{M} \left(1 + \frac{2m_l^2}{M^2}\right) \sqrt{1 - \frac{4m_l^2}{M^2}} \left(\frac{1}{\mathrm{e}^{\frac{q_0}{2T}} + 1}\right)^2 \tag{3.30}$$

Equations (3.24) and (3.30) are seen to be identical. Both this result and our numerical evaluation should not come as a surprise, as the one-loop self energy is known to correspond to a two-body scattering process. As such, we present the above not as new science, but instead as a test of the quantitative validity of our approach to modelling dilepton production from the QGP.

3.2 Dileptons from Vector Mesons

Dilepton emission in heavy ion collisions is not limited to the partonic phase. After hadronization but before freeze-out, lepton pairs created from vector meson decays in the hot hadronic medium are numerous and account for a significant portion of the particle spectra, especially at lower invariant masses. As such, one requires a method of modelling these decays that can later be folded with the fireball evolution. There has been significant research in to the in-medium properties of the ρ, ω and ϕ mesons, not only due of their contribution to the dilepton spectra, but also because observed mass shifts or peak broadening can be perceived as signals of chiral symmetry restoration [23]. Though numerous methods have been proposed to study these effects (see [24] for a review) we choose to employ the "model independent" theory of Eletsky et al. [25] to find the self energy necessary to generate the pair production rate. In this approach, the forward scattering amplitude of ρ and ω (i) mesons with pions and various hadron resonances (a) is found for low energies in the center of mass (CM) frame by

$$f_{ia}^{CM}(s) = \frac{1}{2q_{CM}} \sum_R W_{ia}^R \frac{\Gamma_{R\to ia}}{M_R - \sqrt{s} - \frac{1}{2}i\Gamma_R} - \frac{q_{CM} r_P^{ia}}{4\pi s} \frac{1 + \mathrm{e}^{-i\pi\alpha_P}}{\sin(\pi\alpha_P)} s^{\alpha_P} \tag{3.31}$$

where s is the center of mass energy and the first terms corresponds to a sum over Breit-Wigner resonances with mass M_R and total width Γ_R. The factor W_{ia}^R accounts for a statistical averaging for the spin and isospin of the resonance, meson and scattering particle. The second term considers Pomeron background contribution, which, in combination with a Regge term, is how the scattering amplitude is obtained for higher energies (theoretical details on these contributions are beyond the scope of this work, but see [26] for an overview). The strength of this approach lies in the ability to populate the parameters of f^{CM} with experimentally measured data for the resonances from which the ρ and ω will scatter in the hot hadronic medium, thus circumventing parameterization issues that may arise in methods that utilize effective Lagrangians to determine spectral densities.

Once the forward scattering amplitudes are found, the contribution to the self energy for on shell interactions can be written in the rest from of a as

$$\Pi_{ia}(p) = -\frac{m_i m_a T}{\pi p}\int_{m_a}^{\infty} d\omega \ln\left(\frac{1-\mathrm{e}^{-\frac{\omega_+}{T}}}{1-\mathrm{e}^{-\frac{\omega_-}{T}}}\right) f_{ia}\left(\frac{m_i\omega}{m_a}\right) \tag{3.32}$$

where E and p are the energy and momentum of the meson, $\omega = m_a^2 + k^2$ and $f_i a = \frac{\sqrt{s}}{m_a} f_{ia}^{CM}$. Furthermore, if a is a boson $\omega_\pm = \frac{E\omega \pm pk}{m_i}$. If the scattering particle is a fermion then this term is appended by $-\mu$, accounting for the chemical potential, and the numerator and denominator in the logarithmic term of (3.32) are flipped. Individual contributions sum to give the total self-energy via

$$\Pi_i^{\mathrm{tot}} = \Pi_i^{\mathrm{vac}} + \sum_j \Pi_{j\pi} + \sum_k \Pi_{kN} \tag{3.33}$$

where we are summing over the pions and resonances in the self interaction. The vacuum contribution for the ρ can be found via the method of Gounaris and Sakurai [27]. Dilepton production from this approach is found via vector meson dominance, which states [28] that the hadronic electromagnetic current operator is given by

$$J_\mu = -\frac{e}{g_\rho} m_\rho^2 \rho_\mu - \frac{e}{g_\omega} m_\omega^2 \omega_\mu \tag{3.34}$$

where ρ_μ and ω_μ are the field strengths of the respective mesons. From this operator we can connect the hadronic spectral densities to photon self energy (note that we do not consider contributions from ϕ decays, though work in this regime is currently underway [29]). This allows us to write the dilepton production from decay of vector meson i in terms of the imaginary part of the meson propagator:

$$E_+ E_- \frac{dN}{d^4x d^3p_+ d^3p_-} = \frac{2}{(2\pi)^6}\frac{e^4}{g_i^2}\frac{m_i^4}{M^2}(p_+^\mu p_-^\nu + p_+^\nu p_-^\mu - p_+ p_- g^{\mu\nu}) \mathrm{Im} D_{\mu\nu} \frac{1}{\mathrm{e}^{\frac{E}{T}} - 1} \tag{3.35}$$

with each meson contributing linearly to the total pair production. Finally, we need to relate the imaginary part of the propagator to the known meson self energies, which can be accomplished via [25]

$$\mathrm{Im} D = \frac{\mathrm{Im}\Pi_i^{\mathrm{tot}}}{(M^2 - m_i^2 - \mathrm{Re}\Pi_i^{\mathrm{tot}})^2 + (\mathrm{Im}\Pi_\rho^{\mathrm{tot}})^2} \tag{3.36}$$

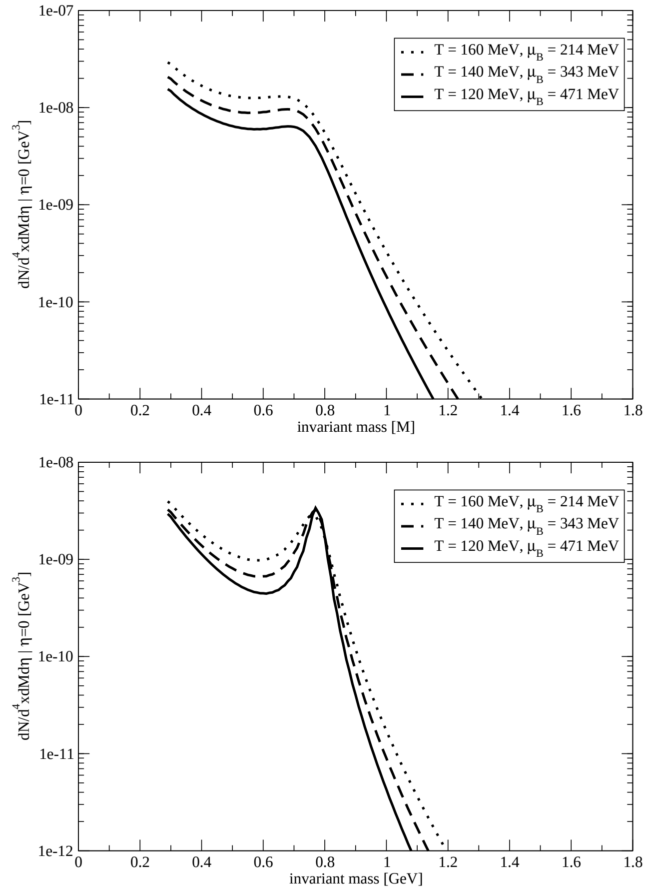

Figure 3.3: Dilepton production rates from the hadronic phase generated using the method of Eletsky et al. at different temperatures. The top panel represents contributions from ρ decays while the bottom is from ω mesons.

The fruits of this method are given in Figure 3.3, which show the dilepton production rates from the ρ and ω mesons. Notice that the in-medium scattering causes significant peak broadening, especially at higher densities and temperatures.

4

Evaluation of Dilepton Spectra

We have now outlined two of the elements found in Eq. (2.1) – the fireball evolution and the particle production rate. In order to address the final step and generate data that can be compared with experimental results, it is necessary to perform numerical calculations. In this chapter we discuss the construction of this program, including an outline of relevant components and implementation of previously discussed techniques, as well as our approach to modelling the CERES detector acceptance.

4.1 The CERES Detector

In order for our results to fit with those seen in CERES experiment it is necessary to model the behaviour of the detector. We begin by presenting a brief overview of the experimental detector setup to motivate the acceptance routine which will be outlined afterwards.

4.1.1 Experimental Setup

Our goal is to model the data collected from 158 GeV per nucleon heavy ion collisions by the CERES experiment at the CERN SPS. CERES is optimized to measure the emission of low invariant mass electron pairs from fixed target p-p, p-A and A-A collisions, utilizing a few apparatuses to detect and gather information on the created particles [5][30][31]. Firstly, the experiment contains two Silicon Drift Chambers (SiDC), used as vertex telescopes to determine the emission angle between the charged pair. Electron-hole pairs are created as a charged particle travels through the semiconducting material. A radial electric field running through the detector causes this

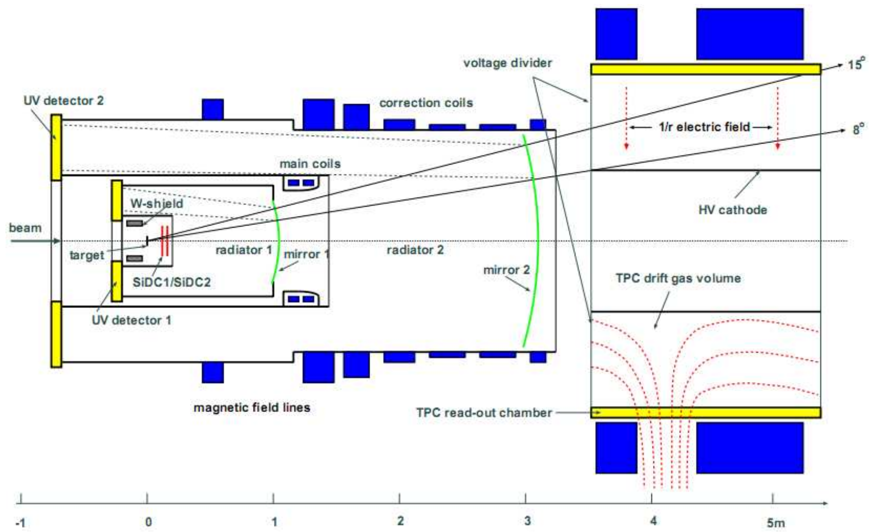

Figure 4.1: A cross section of the CERES spectrometer at the CERN SPS (from [5]).

electron to drift towards an anode, which registers its presence. With the knowledge of the electron's drift velocity through the field as well as the time of its creation, one can reconstruct the trajectory of the particle that created it.

CERES also contains two Ring Imaging Cherenkov detectors (RICH), which help distinguish between dileptons of interest and other particles in the hadronic background which exists after collision. As charged particles travel through the gas mixture in this chamber they cause the emission of Cherenkov radiation, which is subsequently focused by a mirror as a ring on a UV detector.

Finally, post-1998 CERES measurements are aided by a Time Projection Chamber (TPC). The TPC functions similarly to other drift detectors: charged particles cause ionization in the chamber's gas mixture and the resulting electrons drift towards an endcap that converts their existence into an electronic signal. A magnetic field is also present, causing the charged particles to bend and thus facilitating momentum measurements.

The above equipment is used not only to reconstruct the properties of dilepton pairs; they are necessary to discriminate between particles of interest and the massive amount of background created by heavy ion collisions. Each detector aides in this: since the angle between lepton pairs is usually smaller for the frequent γ and Dalitz

(π^0) decays, the SiDC is invaluable in determining relevant hits. Finally, in addition to momentum detection, the TPC can also reconstruct particle energy loss, dE/dx, helpful in distinguishing between electrons and other charged products.

4.1.2 Modelling Detector Acceptance

The CERES detector is optimized to measure dileptons with p_T >0.2GeV in the midrapidity range $2.1 < \eta < 2.65$ with full azimuthal coverage [5]. With this in mind, we choose to model detector acceptance as follows: given the lab frame energy, transverse momentum and rapidity measurement interval ($-\eta_{measure} < \eta < \eta_{measure}$) of virtual photons we can make an initial judgement: if half of its rest frame rapidity lies outside the $\eta_{measure}$ range or the rest frame p_T is below the threshold mentioned above the photon is discarded. If it passes these criteria, we continue by Lorentz transforming the input data to the particle's rest frame and use this to generate energy and momentum for the dilepton pair. Given that CERES has equal resolution over all azimuthal angles, there is no need to discriminate against dilepton trajectory. As such, to best model the process of pair creation from the virtual photon, we require a random distribution of lepton pairs from the virtual photon over a spherical surface in order to imitate the behaviour of the experiment. This is accomplished by pseudo-randomizing the dilepton parameters in $\phi, \cos\theta$ and $\sin\theta$. Once generated, the kinematical quantities are transformed back to the lab frame wherein they are tested against the acceptance criteria again. If either lepton does not fall within the parameters the pair is thrown out. The process is repeated for a given number of iterations for every set of input data, each time tracking whether or not the virtual photon/lepton pair passes scrutiny. This quantity is easily transformed into a probability, applied to each virtual photon produced by the evolution, providing a reasonable model of the detector acceptance.

Figure 4.2 shows the effect of the acceptance Monte Carlo on the dilepton pair rates measured by the program, with other variables fixed and assuming the parent virtual photon has passed initial checks. Unsurprisingly, the rapidity dependence is symmetric, with dileptons emitted at midrapidity having the highest probability of

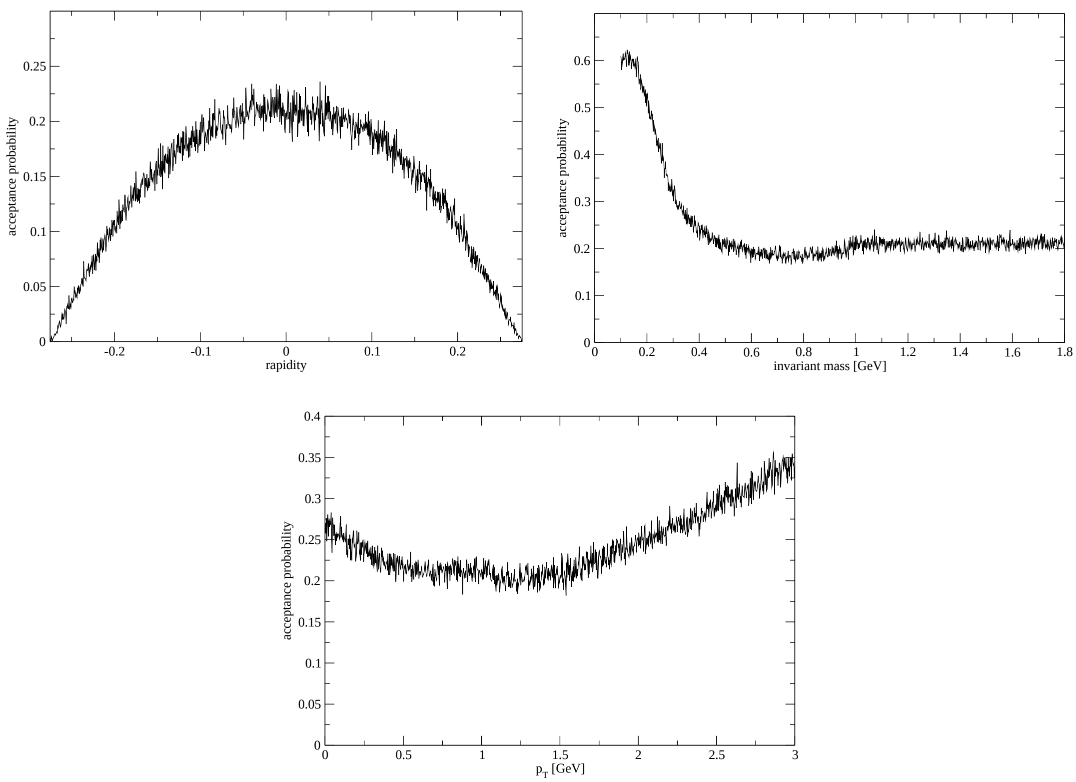

Figure 4.2: Probability of dilepton pair passing acceptance checks, by initial virtual photon rapidity (top left), invariant mass (top right) and p_T (bottom). In all three plots the mass is set at 1 GeV, rapidity at 0 and p_T at 1 GeV, except when the probability dependence of that variable is being calculated.

being counted. The products of photons that stray away from $\eta = 0$ are less likely to be counted given the decreasing likelihood of both leptons falling within the CERES detector rapidity range.

The mass dependence presents a more complicated scenario. For low M, discarded counts are dominated by cases of insufficient transverse momentum. As the mass increases, rapidities outside of the detector range become more prominent while p_T rejections are still fairly numerous. The momentum cuts eventually become exceedingly rare and η cuts level off, leading to the equilibrium visible for higher masses.

A similar trend presents itself when analyzing changes in p_T, although the causes are different. Initially, leptons outside of the rapidity range are responsible for the majority of discarded data. As the photon transverse momentum increases so do the number of leptons under the p_T threshold until the momentum becomes large enough to ensure that most pairs pass this criteria. At the same time, increasing p_T results in a decreasing variance in product rapidity and as result we find that the acceptance probability increases in this region.

4.2 Space-Time and Four-Momentum Integration

Up until this point, when discussing pair production we have quoted the formulae in terms of differentials in spacetime and particle four-momentum. As previously noted, dilepton emission occurs over the entire lifetime of the fireball, thus necessitating a description of the time evolution. Furthermore, experimental techniques cannot always discern certain dilepton properties, such as transverse momentum, to a high degree of precision. Clearly it is not sufficient to generate particle rates dependent on these quantities. Instead we must collect our results over the entire space-time interval as well as over the extent of certain kinematical quantities. Utilizing the transformations $d^4x = \tau r d\tau dr d\phi d\eta_s$ and $d^4p = M p_T dM dp_T d\eta d\psi$, this may be accomplished by performing the integration (as in [4])

$$\begin{aligned}\frac{dN}{dM} = \frac{2\pi M}{\Delta\eta}\int_{\tau_0}^{\tau_f}\tau d\tau\int_0^{R(\tau)} r dr\int_{-\eta_s^{front}(\tau)}^{\eta_s^{front}(\tau)} \mathrm{V}(\eta_\mathrm{s},\mathrm{T}) d\eta_s\int_0^{2\pi} d\psi \\ \times\int_{\eta_{min}}^{\eta_{max}} d\eta\int_0^{\infty} p_T dp_T\frac{dN(M,p_T,\eta,T)}{d^4x d^4p}\mathrm{Acc}(M,p_T,\eta)\end{aligned} \tag{4.1}$$

with τ the proper time, η_s the spacetime rapidity of the fireball (which should not be confused with η, the emitted virtual photon rapidity) and $\mathrm{Acc}(M, p_T, \eta)$ the acceptance function. The ϕ contribution has been integrated out due to the cylindrical symmetry assumed in the fireball and we are averaging over the detector rapidity range $\Delta\eta$. Many of the integration bounds are subjective, with only the requirement that they be large enough to capture the extent of the evolution we utilize. In our calculations, the fireball is constrained to within a radius of 0 fm$< R <$10 fm and spacetime rapidity interval $-2 < \eta_s < 2$ with a lifetime (that is, time from equilibration to freeze-out) of 0.6 fm/c$< \tau <$15 fm/c.

In order to evaluate Eq. (4.1) it is necessary to implement the third party integration routines contained in the Cuba library [32]. While this package contains four different multidimensional integration algorithms, only two, Vegas and Divonne, are used to any significant degree. We will briefly outline these routines here.

The Vegas routine uses a pseudo- or quasi-random sample and importance sampling to converge on a solution [33]. The algorithm begins by creating an evenly distributed set of steps over the integration volume. The integrand is evaluated at random coordinates and the results are compiled into a weight function used to create an updated distribution in which the steps are of a smaller width around areas where the integrand is of large absolute magnitude. This process is continued iteratively, each time increasing the resolution at the points which contribute most strongly to the integration and in turn reducing the variance until an acceptable level of error is reached.

Divonne's approach, known as stratified sampling, holds similarities to importance sampling but is different in a few important ways [34]. Assuming a simply bounded multidimensional region (a condition that can be satisfied by a change of variables),

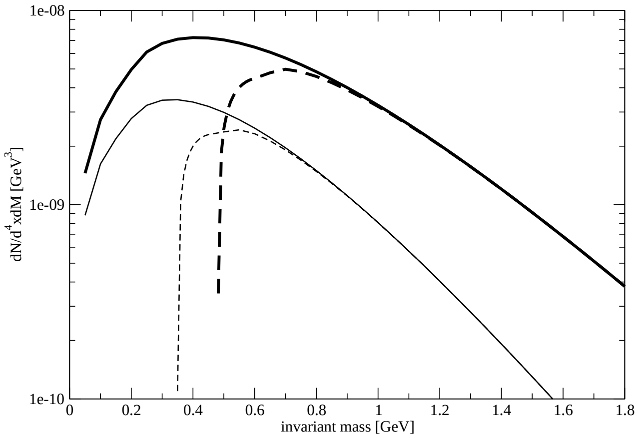

Figure 4.3: Effect of thermally generated quark masses on dilepton mass rate in the QGP phase. The solid lines represent the spectra generated from quarks with only bare mass while the dashed lines comes from quarks with thermal masses. The thick lines were computed at a temperature of $T = 255$ MeV and the thin lines at $T = 200$ MeV.

the Divonne algorithm begins by analyzing the misbehaviour of the integrand over a given region (initially the entire bounds of integration). It computes the difference between the maximum and minimum points in this bound and gives a weight to the misbehaviour, called the spread. Regions with a significant rate of change per volume, i.e. a large spread, are prioritized for further subdivision. Variance is minimized by continuing this process until all regions contain approximately equal spread, at which point the integral is evaluated in each division.

The main difference between Vegas and Divonne lies in their methodology of division of the integral bounds. Divonne places importance on both the absolute magnitude of the integrand as well as the rate of change of the function within a region while Vegas focuses only on the former. For our purposes, both routines converged to the same values, but as Divonne did so in a significantly shorter time it became the preferred choice, with Vegas being utilized mostly for numerical checks of Divonne's work.

4.3 Implementing the Quasiparticle and Evolution Models

Little work is needed to implement the quasiparticle description of the QGP in our study of dilepton emission. Obviously, the equation of state that stems from this interpretation has an enormous bearing on the evaluation of the fireball evolution, but its macroscopic effects on the pair spectra is limited to the substitution of thermal quark masses (see Eq. (2.3)) for bare masses in the photon self-energy. The effect of these thermal masses can be seen in Figure 4.3, which illustrates the QGP phase contribution to the differential dilepton mass spectra – independent of the space-time evolution of the post collision volume. The rates show that the temperature dependence leads to a cut off of dilepton emissions at significantly higher invariant virtual photon mass than in the case of bare quarks. This is intuitive as the annihilation of heavier quarks will produce more energetic photons. As the temperature approaches T_C, the dilepton rate cutoff closes in on twice the bare quark mass, an effect which is mirrored in higher temperature cases where the cutoff resides at twice the thermal quark mass. Also note that the two cases converge for high invariant masses, where the momentum of the quark pair begins to overshadow the effect of thermal masses.

Given the computation power required, we integrate the evolution model into numerical calculations not by direct evaluation but instead by utilizing a pre-prepared data file. This gives us a grid, equidistant over τ, η_s and r (with step sizes 0.14545 fm/c, 0.21053 and 0.169492 fm, respectively), containing the fireball's temperature, radial velocity, longitudinal rapidity and baryon chemical potential for a 5% central Pb-Pb collision at 158 GeV/nucleon. We assume smooth changes in these properties over the grid, so linear interpolation is used to determine the fireball physics at the point(s) of interest.

4.4 Generating Dilepton Rates

Given the fairly straightforward mathematics, dileptons rates in the QGP phase are calculated on-the-fly via (3.1). Input variables are either user generated, generated dynamically by the integration routine, or determined by evolution data. This gives us the kinematics of the virtual photon, which are then folded with acceptance.

Below the transition temperature, lepton pairs from mesons are generated similarly, except we found it advantageous to store the $\mathrm{Im}\overline{\Pi}$ data in a static file, as was done with the evolution. The spectral data is given per an equidistant grid of $M, |\mathbf{p}|, T$ and μ_B (with step sizes 20 MeV, 99.71 MeV, 5 MeV and 30.3 MeV, respectively) where we again use linear interpolation to determine information that falls between the given points.

A significant amount of research has been done (see, for example, [35]) in hopes of classifying the nature of the QGP phase transition, but determining the transition order in such a complex system has proven difficult and thus far no consensus has been reached. Given this, we assume a crossover transition, that is, we ignore the possible existence of a mixed partonic/hadronic phase, instead immediately switching dilepton production from quark-antiquark annihilation to vector meson decay at T_C, which, in our model, occurs at 170 MeV.

Dileptons are also produced after freeze out (set at $T_f = 100$MeV in our calculations) from vacuum decays of the remaining vector mesons. Dalitz decays, that is, $\pi^0 \rightarrow e^+ + e^- + \gamma$, are dominant the low mass ($M < 400$ MeV) region of the spectra, though contributions also come from vacuum ρ, ω and ϕ mesons. Collectively, dileptons from this phase are referred to as the *cocktail*. Since these decays are not in-medium, resulting pair production is not governed by the processes discussed in Chapter 3 and we must rely on particle spectra data gathered by the CERES collaboration to account for post-freeze out contributions.

4.5 Results

The main result of our work is given in Figure 4.4, which presents the dilepton invariant mass spectrum generated using the fireball model folded with detector acceptance. Though the evolution is evaluated for a Pb-Pb collision, we compare our results to data from CERES Pb(158AGeV)-Au experiments [36], as the mass of the parent nuclei should be similar enough as to provide a sufficient comparison. However, it is necessary to scale our data by the average number of charged particles, $< N_{ch} >$, which for the 7% most central Pb-Au events at CERES is 177 [36].

Our results agree fairly well with experimentally measurements. For invariant masses below $M = 1.0$GeV the spectrum is heavily influenced by vector meson decays and the cocktail. Calculations fall slightly below experiment in the region surrounding $M = 0.9$GeV, but this result is not surprising as our analysis neglects contributions for in-medium ϕ meson decays whose broadened peak is expected to seen around this mass. For higher masses, the cocktail and meson contributions die off, leaving $q\overline{q}$ annihilations as the main source of lepton pairs. Again we see good agreement, but the large uncertainty in this region makes it difficult to declare with conviction that the QGP has been formed at the SPS.

A check of the dilepton spectra from the QGP phase is presented in Figure 4.5, which compares the results generated by the two methods discussed in Chapter 3. The field theory approach, which was used to calculate the total rate in Figure 4.4, is close to kinetic theory results for low invariant masses. Above about 0.8 GeV the spectra diverge, with Kajantie et al.'s lepton production falling significantly below our results. This is not concerning, however, as we merely use this comparison to ensure that our dilepton spectra evaluation is well implemented, which the reasonable behaviour of the kinetic theory approach corroborates. Note also that despite the gap that exists for higher invariant mass, the results of Kajantie et al. still fall well within the experimental uncertainty of CERES data in this region.

Figure 4.6 gives an overview of how our detector acceptance model affects measured dilepton production over the lifetime of the evolution. The partonic and hadronic contributions both show similar trends, with acceptance causing a fairly consistent order of magnitude drop in pair counts for masses above 700 MeV. Below this the difference is slightly larger, which we surmise is caused by the tendency for dileptons to fall below the transverse momentum threshold in this region. The consistency observed for higher masses mirrors the results presented in Chapter 3 where it was found that acceptance probability approaches a constant in for higher input invariant mass. We also observe that the acceptance behaves similarly between our two QGP techniques (Figure 4.5), further indicating the stability of our calculations in this phase.

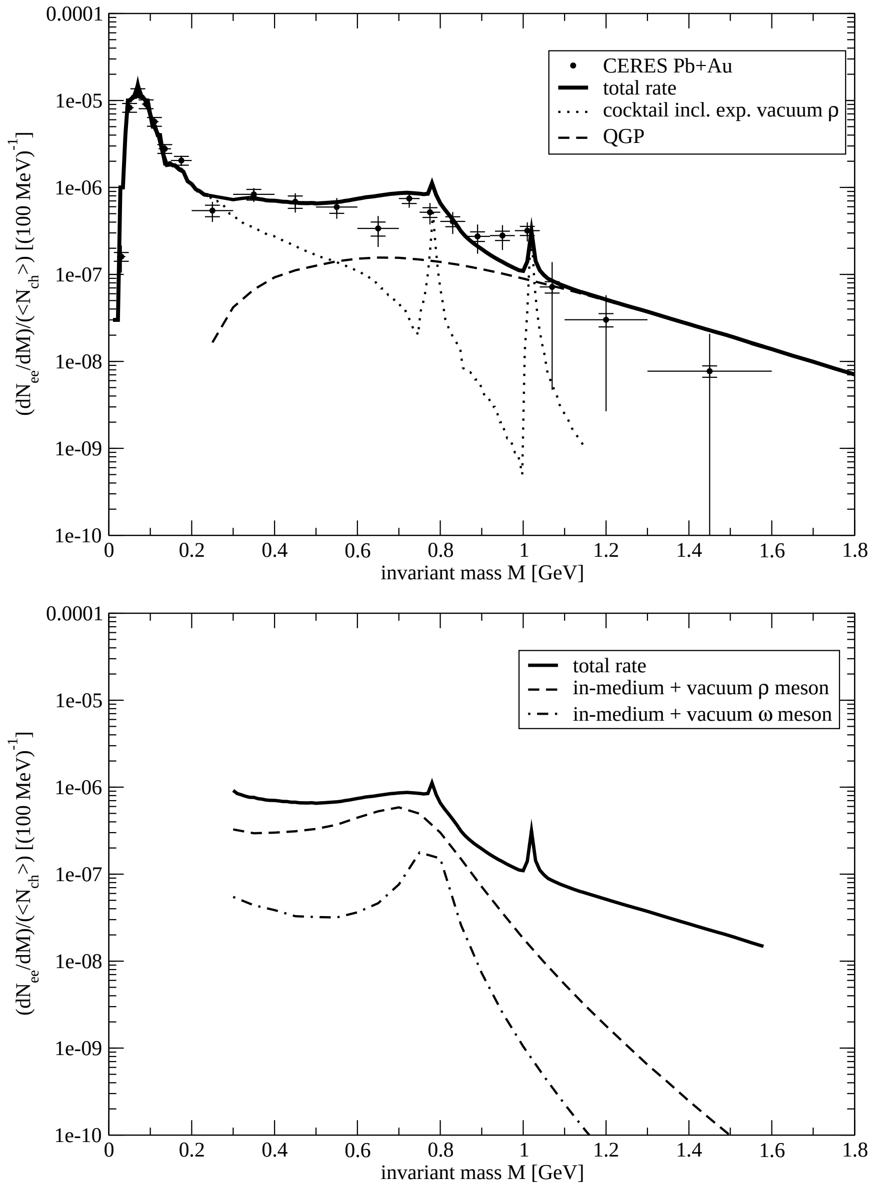

Figure 4.4: (Top) Dilepton invariant mass spectra scaled by $< N_{ch} >= 177$ using Pb(158 AGeV)-Pb evolution. The total rate (including QGP, in-medium and vacuum ρ and ω mesons and the hadronic cocktail) is compared with the QGP contribution and data from CERES Pb(158AGeV)-Au experiments. Cocktail data is not available for $M > 1.14$ GeV, so the total rate above this mass consists of only the QGP and vector meson contributions. (Bottom) Dilepton spectra contributions from the in-medium and vacuum ρ and ω mesons from the hadronic phase, compared to the total rate.

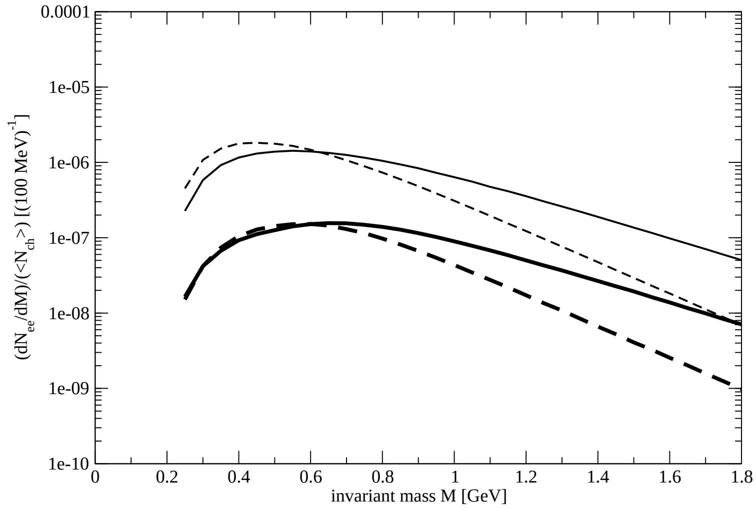

Figure 4.5: Comparison of QGP contribution to invariant mass spectra using the different methods presented in Chapter 2: using finite temperature field theory and a Dirac particle distribution to find the imaginary photon self energy (solid line) and using kinetic theory and a Maxwell particle distribution (dashed line). Calculations with acceptance are represented by thick lines while those without acceptance are thin lines.

The importance of a strong acceptance model is demonstrated in Figure 4.7, which sums the results presented in Figure 4.6, as well as the cocktail contribution, and compares this to CERES Pb-Au data. The calculated spectra is significantly above experimental measurements for the entire range of invariant mass – enough that ω and ϕ peaks from the cocktail are almost indistinguishable.

Our choice of evolution model gives us the ability to generate a differential p_T dilepton spectra, as given in Figures 4.8 and 4.9. Though its shape follows the expected profile, due the low resolution of the CERES detector in p_T (in this centrality class) there is no experimental data with which this can be closely compared, leaving the result as a prediction to be tested by future experiments.

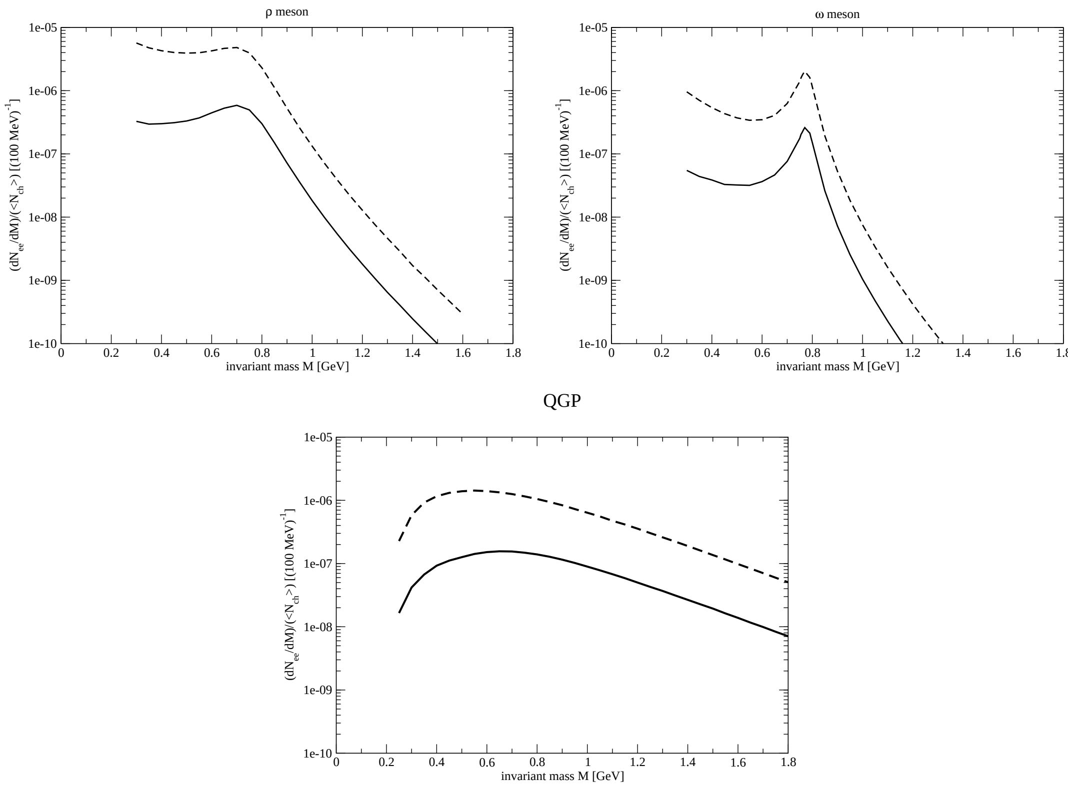

Figure 4.6: Dilepton invariant mass spectra with (full line) and without (dashed line) acceptance for the in-medium and vacuum (top left) ρ and (top right) ω mesons as well as the (bottom) QGP contribution.

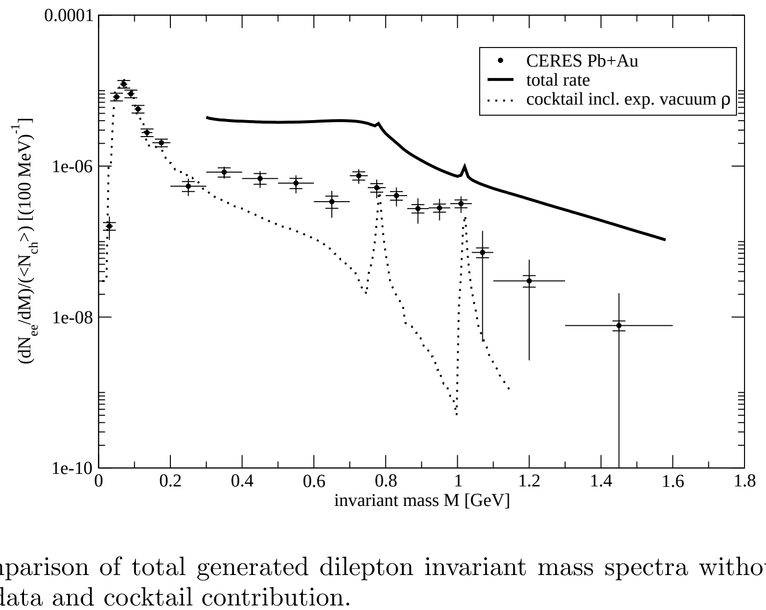

Figure 4.7: Comparison of total generated dilepton invariant mass spectra without acceptance to CERES Pb-Au data and cocktail contribution.

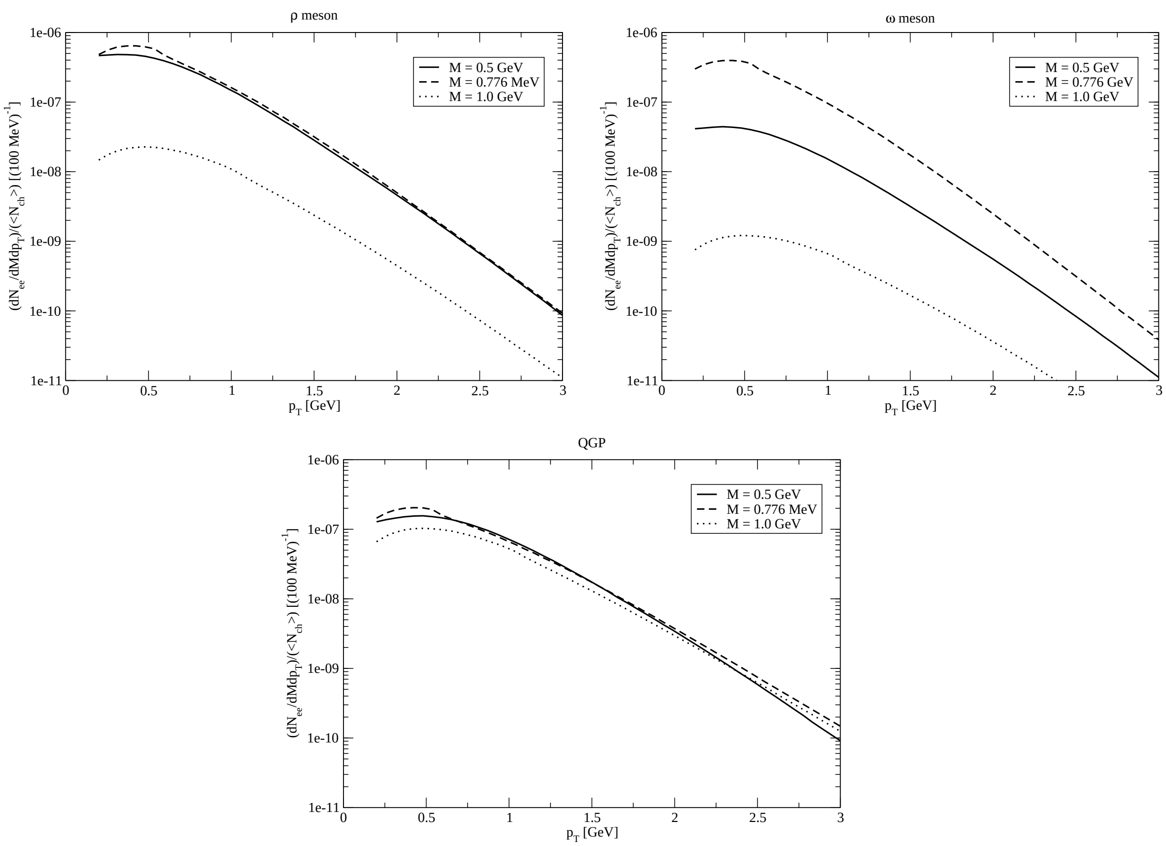

Figure 4.8: Theoretical predictions for particle spectra differential in invariant mass and transverse momentum with varying masses for the in-medium and vacuum (top left) ρ and (top right) ω mesons as well as the (bottom) QGP contribution.

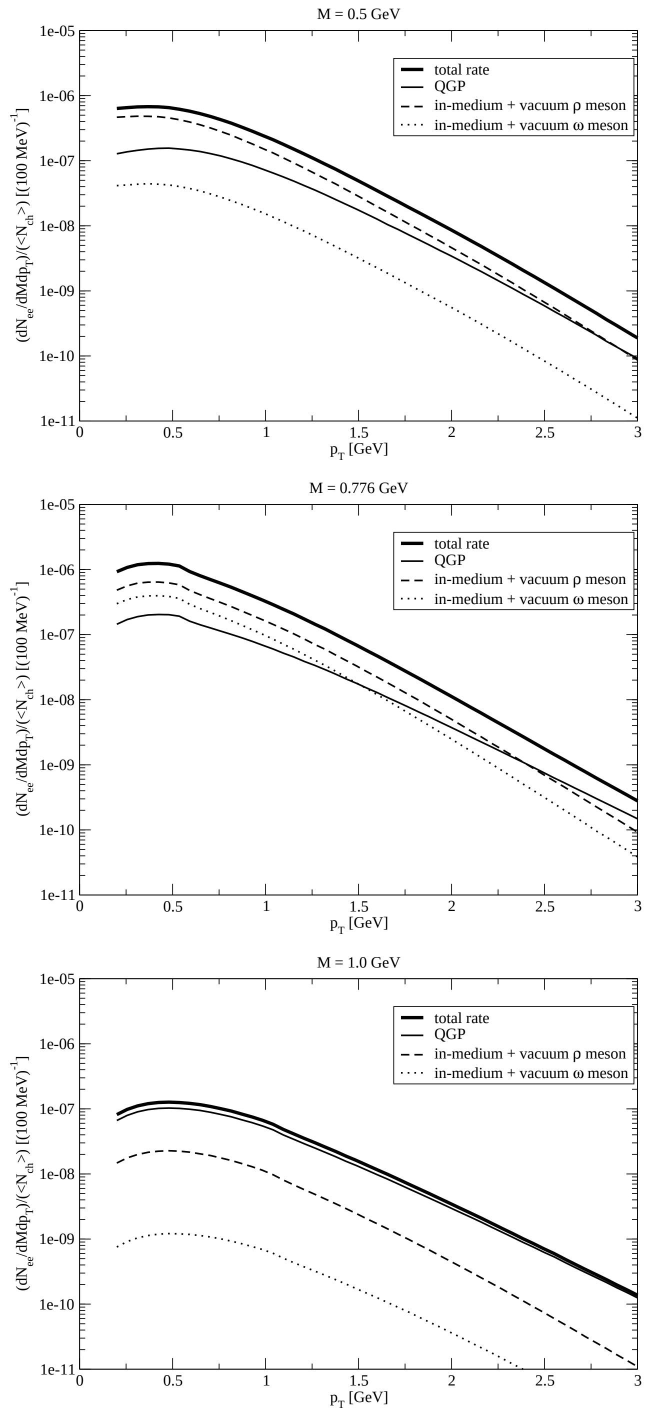

Figure 4.9: Theoretical predictions for total particle spectra differential in invariant mass and transverse momentum with $M = 0.5$GeV (top), $M = 0.776$GeV (middle) and $M = 1.0$GeV (bottom panel). Note that the total rates shown here does not include any cocktail contribution.

5

Summary and Conclusions

We have analyzed the production of dileptons from the collision of lead and gold nuclei with energies of 158 GeV/nucleon by the CERES experiment at the CERN SPS. We are able to describe an equation of state that mirrors lattice QCD results in the early life of the system by considering the quarks and gluons as quasifree particles with thermally generated effective masses. After confinement sets in, the thermodynamics are obtained by a combination of experimental data as well as conservation of baryon number and isentropic expansion, which allowed us to interpolate the EoS from the point of freeze-out back to the phase transition. The evolving system is described by a equilibrated, cylindrically symmetric volume undergoing accelerated expansion. Such a model forgoes a microscopic description of the evolving system as presented in hydrodynamical descriptions in favour of one which accurately reproduces a large set of observables. Though we utilize a collision evolution that assumes an initial Pb-Pb collision, the similar nuclei size and centrality class makes it suitable to compare our results to CERES Pb-Au experiments. Dilepton production in the QGP phase is found from the photon self energy via finite temperature field theory techniques. Along the way, we reproduce, numerically and analytically, the well-known equality of first order field theory and kinetic theory techniques when describing two body scattering. After hadronization, the spectral densities of in-medium mesons are found by utilizing experimental scattering data of these particles with pions and hadron resonances.

The above conditions are folded with a model of the CERES detector acceptance and numerically evaluated over the entire lifetime of the collision to produce dilepton spectra. Comparing our results with experimental data yields good agreement: in the low mass region ($M < 1GeV$), pair production is strongly influenced by the cocktail, however, measurements from collision cannot be reproduced without considering meson decays from a thermalized hadronic medium as well as $q\overline{q}$ annihilation in a strongly interacting system of deconfined quarks and gluons. This observation is strengthened when analyzing higher mass regions; as in-medium and cocktail hadronic decays die off, the dilepton spectra becomes dominated by QGP contributions which fit very well with CERES data.

The only problematic region of the invariant mass spectrum is that spanning 0.9GeV $< M <$ 1.0GeV where our results are consistently below that of the CERES experiment. We surmise that this discrepancy is due to our neglect of dileptons from ϕ meson decays. It is believed that in the hadronic medium the ϕ will undergo significant peak broadening, making its contribution in this mass range quite significant. Over the course of our work there was an insufficient research into generating its spectral densities using the methods utilized for ρ and ω, however, recent studies [29] will likely allow us to include the contribution of ϕ decays in future work.

The agreement of our calculations with Pb-Au collision data serves as testament to the power of the fireball evolution model proposed by Renk. It has now be shown to accurately reproduce results from both the NA60 [11] and CERES, two experiments with strikingly different collision dynamics. On a larger level, our findings bode well for the current understanding of heavy ion experiments. Hadronic contributions in low mass regions as well as the dominance of QGP calculations for higher invariant mass can be construed as adding to the mounting evidence for the creation of a strongly interacting partonic plasma at the CERN SPS, however, our work, like so many others', has not yielded incontrovertible proof. It nevertheless constitutes an important milestone which, together with similar analyses of measurements at RHIC and soon at the LHC, will enable us to realize the full potential of electromagnetic observables in high energy nuclear collisions.

Bibliography

[1] S. B. Ruester, V. Werth, M. Buballa, I. A. Shovkovy, and D. H. Rischke, Phys. Rev. **D72**, 034004 (2005), hep-ph/0503184.

[2] P. Salabura, Acta Phys.Polon. **B39**, 307 (2008).

[3] T. Renk, R. A. Schneider, and W. Weise, Phys. Rev. **C66**, 014902 (2002), hep-ph/0201048.

[4] T. Renk, J. Phys. **G30**, 1495 (2004), hep-ph/0403239.

[5] CERES, A. Marin *et al.*, PoS **CPOD07**, 034 (2007), 0802.2679.

[6] L. D. McLerran and B. Svetitsky, Phys. Rev. **D24**, 450 (1981).

[7] J. P. Lansberg, Int. J. Mod. Phys. **A21**, 3857 (2006), hep-ph/0602091.

[8] S. Soff, J. Phys. **G30**, S139 (2004), nucl-th/0312085.

[9] J. D. Bjorken, K. L. Kowalski, and C. C. Taylor, (1993), hep-ph/9309235.

[10] U. W. Heinz, (2004), hep-ph/0407360.

[11] J. Ruppert, C. Gale, T. Renk, P. Lichard, and J. I. Kapusta, Phys. Rev. Lett. **100**, 162301 (2008), 0706.1934.

[12] T. Renk and J. Ruppert, arXiv (2006), hep-ph/0605130.

[13] P. Levai and U. W. Heinz, Phys. Rev. **C57**, 1879 (1998), hep-ph/9710463.

[14] R. A. Schneider and W. Weise, Phys. Rev. **C64**, 055201 (2001), hep-ph/0105242.

[15] J. I. Kapusta and C. Gale, *Finite-Temperature Field Theory: Principles and Applications* , Cambridge, UK: Univ. Pr. (2006) 428 p.

[16] A. Peshier, B. Kampfer, and G. Soff, Phys. Rev. **C61**, 045203 (2000), hep-ph/9911474.

[17] P. Huovinen and P. V. Ruuskanen, Ann. Rev. Nucl. Part. Sci. **56**, 163 (2006), nucl-th/0605008.

[18] T. Renk, Phys. Rev. **C68**, 064901 (2003), hep-ph/0210307.

[19] P. Braun-Munzinger, K. Redlich, and J. Stachel, (2003), nucl-th/0304013.

[20] P. Braun-Munzinger, J. Stachel, J. P. Wessels, and N. Xu, Phys. Lett. **B344**, 43 (1995), nucl-th/9410026.

[21] K. Kajantie, J. I. Kapusta, L. D. McLerran, and A. Mekjian, Phys. Rev. **D34**, 2746 (1986).

[22] M. E. Peskin and D. V. Schroeder, *An Introduction to Quantum Field Theory* , Reading, USA: Addison-Wesley (1995) 842 p.

[23] J. W. Harris and B. Muller, Ann. Rev. Nucl. Part. Sci. **46**, 71 (1996), hep-ph/9602235.

[24] R. Rapp and J. Wambach, Adv. Nucl. Phys. **25**, 1 (2000), hep-ph/9909229.

[25] V. L. Eletsky, M. Belkacem, P. J. Ellis, and J. I. Kapusta, Phys. Rev. **C64**, 035202 (2001), nucl-th/0104029.

[26] P. D. B. Collins, *An Introduction to Regge Theory and High-Energy Physics* , Cambridge 1977, 445p.

[27] G. J. Gounaris and J. J. Sakurai, Phys. Rev. Lett. **21**, 244 (1968).

[28] C. Gale and J. I. Kapusta, Nucl. Phys. **B357**, 65 (1991).

[29] G. Vujanovic, J. Ruppert, and C. Gale, *In preparation* .

[30] CERES, G. Hering, (2001), nucl-ex/0203004.

[31] CERES, R. Baur *et al.*, Z. Phys. **C71**, 571 (1996).

[32] T. Hahn, Comput. Phys. Commun. **168**, 78 (2005), hep-ph/0404043.

[33] G. P. Lepage, J. Comput. Phys. **27**, 192 (1978).

[34] J. H. Friedman, ACM Trans. Math. Software **7**, 76 (1981).

[35] D. Kumar Srivastava and C. Gale, Phys. Lett. **B319**, 407 (1993), hep-ph/9311267.

[36] D. Adamova *et al.*, (2006), nucl-ex/0611022.